



# Onion-like carbon-embedded graphitic carbon nitride for enhanced photocatalytic hydrogen evolution and dye degradation

Yuxi Shi <sup>a,b</sup>, Qi Zhao <sup>a,\*</sup>, Jiayin Li <sup>a,b</sup>, Guanyue Gao <sup>a,b</sup>, Jinfang Zhi <sup>a,b,\*\*\*</sup>

<sup>a</sup> Key Laboratory of Photochemical Conversion and Optoelectronic Materials, Technical Institute of Physics and Chemistry, Chinese Academy of Sciences, Beijing 100190, PR China

<sup>b</sup> University of Chinese Academy of Sciences, Beijing 100049, PR China



## ARTICLE INFO

### Keywords:

Onion-like carbon  
Graphitic carbon nitride photocatalyst  
 $Sp^2/Sp^3$  ratio  
Hydrogen evolution

## ABSTRACT

Limited light absorption and low charge separation rate are the main obstacles for graphitic carbon nitride ( $g\text{-C}_3\text{N}_4$ )-based photocatalyst. Here, onion-like carbon (OLC), a carbon nanostructure with multilayer graphitic shells, was embedded into the  $g\text{-C}_3\text{N}_4$  matrix to enhance the photocatalytic performance. Due to its high degree of  $Sp^2$  hybridization and good electrical conductivity, the OLC can broaden visible light adsorption, narrow the band gap of  $g\text{-C}_3\text{N}_4$ , and serve as electron acceptor to promote the separation of photo-generated carrier. Thus, the  $g\text{-C}_3\text{N}_4/OLC$  composites show an increased hydrogen evolution rate of  $3086 \mu\text{mol g}^{-1} \text{h}^{-1}$ , 4.44 times higher than pure  $g\text{-C}_3\text{N}_4$ . Furthermore, the  $H_2$  evolution rate is highly related to the  $Sp^2/Sp^3$  ratio of OLC. In addition, efficient photocatalytic degradation of RhB was also achieved ( $0.1171 \text{ min}^{-1}$ ). The photocatalytic mechanism was then elucidated through a series of spectrochemical and photochemical test. This work demonstrates the significant applicability of OLC in designing carbon-based photocatalyst with highly-efficient photocatalytic activity towards future solar energy conversion and pollutants degeneration.

## 1. Introduction

With the crisis of energy and environment, photocatalysis has been regarded as a promising solution to produce hydrogen ( $H_2$ ) from water and to degrade organic pollutants by using solar energy [1]. Exploration of efficient and 'green' photocatalysts is the key to this sustainable technology. As a polymeric semiconductor, carbon nitride ( $g\text{-C}_3\text{N}_4$ ) has received extensive acceptance due to its metal-free nature, appropriate band energy position, chemical stability and low production cost [2–4]. However, pure  $g\text{-C}_3\text{N}_4$  suffers from lower photocatalytic efficiency compared to metals or metals oxides [5]. The main issues include: (i) the larger bandgap of  $g\text{-C}_3\text{N}_4$  limits light absorption in visible range; (ii) the low charge mobility of polymer impedes charge transfer and separation; (iii) the stacking of the polymeric layers leads to relatively low specific-surface areas, et al. Much effort has been devoted to addressing these drawbacks to improve photocatalytic performance [6–10]. The typical approach was to construct heterostructure [11] by coupling semiconductor (i.e., transition metal oxides [12,13], sulfides [14,15], noble metal (i.e., Ag [16], Pt [17], Pd [18]), and other extraneous

material. The main problem of metal-containing photocatalysts is leaching of toxic metals in practical applications. By comparison, carbon-based materials have competitive properties including abundant sources and environmental friendliness, as well as diverse morphology and tunable structures. In particular, they have enhanced light capture ability in visible range and possess electron transfer and charge reservoir properties [19,20], thereby increasing the photocatalytic activity of  $g\text{-C}_3\text{N}_4$ . Motivated by these advantages, constructing carbon-implanted  $g\text{-C}_3\text{N}_4$  is highly prospective for large-scale photocatalytic applications [21–23].

Up to now, zero-dimensional carbon dots (CDS) and graphene quantum dots (GQDs) were intensively studied to modify  $g\text{-C}_3\text{N}_4$  due to their small size and presence of  $\pi$ -conjugated structure. [24,25]. For instance, Zhang et al. developed a homogenous "spot-heating" synthesis method to implant carbon dots on  $g\text{-C}_3\text{N}_4$  sheets for enhanced solar hydrogen evolution [26]. However, the typical CDS synthesized from the common bottom-up approach [27,28] usually have complex surface functionalities, intrinsic structural defects, and high extent of amorphous domain. The undefined structure, excessive defects, and

\* Corresponding author.

\*\* Corresponding author at: Key Laboratory of Photochemical Conversion and Optoelectronic Materials, Technical Institute of Physics and Chemistry, Chinese Academy of Sciences, Beijing 100190, PR China.

E-mail addresses: [qizhao@mail.ipc.ac.cn](mailto:qizhao@mail.ipc.ac.cn) (Q. Zhao), [zhi-mail@mail.ipc.ac.cn](mailto:zhi-mail@mail.ipc.ac.cn) (J. Zhi).

formation of molecular fluorophores might contribute to the recombination of photoinduced charges, eventually decreasing the number of the free carriers for photocatalysis [20,29,30]. In addition, low production efficiency, cumbersome purification methods and low energy efficiency ratio also limit the large-scale preparation of carbon dots. For the purpose of improving photocatalytic activity of g-C<sub>3</sub>N<sub>4</sub>, the introduced carbon components should meet the requirements: (i) having sufficiently high conductivity to enhance transfer charge; (ii) being embedded in the layers homogeneously without destroying the g-C<sub>3</sub>N<sub>4</sub> matrix. Previous studies proposed that the electrical conductivity and light capture ability of carbonaceous materials were strongly related to the sp<sup>2</sup>-hybridized carbon fraction [31]. A high ratio of sp<sup>2</sup>-hybridized carbon results in an increase of the density states of conductive electrons, and furthermore enhanced the intrinsic conductivity [32]. Besides, the particle size and surface functionalities of carbon components are essential for the solubility in aqueous media, as well as their distribution in g-C<sub>3</sub>N<sub>4</sub> sheets. Considering these issues, developing alternative carbon nanoparticles with small size and high degree of sp<sup>2</sup> hybridization is of significance to fabricate g-C<sub>3</sub>N<sub>4</sub>/carbon hybrids with high photocatalytic performance.

Onion-like carbon (OLC), a relatively new member of the carbon-based nanomaterials, consists of fullerene-like carbon shells enclosed by concentric graphitic shells. It is commonly synthesized by high-temperature (> 1000 °C) graphitization of nanodiamond (NDs) in an inert environment or vacuum [33–35]. During the thermal annealing process, the sp<sup>3</sup>-hybridized carbon atoms on diamond surface rearrange to form graphitic sp<sup>2</sup>-hybridized carbon shells. The obtained NDs-derived OLC is characterized by small size (<10 nm), large surface/volume ratio, and high electrical conductivity [36]. Due to its highly symmetric structure, OLC is considered to exhibit different properties from other nanocarbon (such as graphite, nanotubes, or carbon dots) and have found applications in the fields of catalysis [37–40], energy storage [41–43], machinery [44], etc. Liu et al. loaded amounts of single-atom platinum on the surface of OLC for study of electrocatalytic hydrogen evolution reactions, which demonstrated that small-sized bent OLC could enhance electron accumulation [45]. David et al. deposited a layer of OLC on gold current collectors for the preparation of micro-supercapacitor by electrophoresis that exhibited excellent charge storage capacity [46]. With respect to photocatalysis, the high degree of sp<sup>2</sup> carbon ordering and the abundant surface functional groups could endow the OLC with a broad absorption spectrum and enhanced electrical conductivity, leading to good utilization of solar energy and fast separation of electron-hole [47]. Thanks to its simple and effective synthesis method, high preparation efficiency and low cost, onion carbon is particularly attractive. We envision that OLC was a promising candidate to be coupled with g-C<sub>3</sub>N<sub>4</sub> to improve the photocatalytic performance.

Herein, we fabricated OLC-embedded g-C<sub>3</sub>N<sub>4</sub> composites by in-situ thermal polymerization. The multilayer graphitic shells of OLC don't only enhance light capture efficiency and electrical conductivity of the g-C<sub>3</sub>N<sub>4</sub>, but also acts as electron acceptor to promote the separation of photo-generated carrier. The band gap of g-C<sub>3</sub>N<sub>4</sub> was narrower after OLC embedding, evidenced by density functional theory calculation and UV-Vis diffuse reflectance spectra. Hydrogen evolution and dye degradation efficiency of g-C<sub>3</sub>N<sub>4</sub>/OLC samples under visible light were importantly increased compared to that of pure g-C<sub>3</sub>N<sub>4</sub>. This work demonstrates that OLC, as a novel carbon-based nanostructure, is a highly promising photoelectric material for the synthesis of high-efficiency photocatalysts.

## 2. Experimental section

### 2.1. Materials

Urea, chloroplatinic acid hexahydrate (H<sub>2</sub>PtCl<sub>6</sub>·6 H<sub>2</sub>O), triethanolamine(TEOA), rhodamine B (RhB), p-benzoquinone (BQ), isopropyl

alcohol (IPA) and sodium oxalate(Na<sub>2</sub>C<sub>2</sub>O<sub>4</sub>) were obtained from Macklin Biochemical Co., Ltd. (Shanghai, China) and used without further purification. NDs detonation particles is purchased from Foshan Risun Group Co., Ltd. (Foshan, China). The graphene is purchased from The Sixth Element Materials Technology Co., Ltd. (Changzhou, China) and Carbon Quantum Dots (CQDs, XF253) is purchased from Nanjing XFNANO Materials Tech Co., Ltd. (Nanjing, China) without further treatment. Ultrapure (Milli-Q) water was used to prepare all solutions and in the photocatalytic hydrogen production tests.

## 2.2. Synthesis of catalysts

### 2.2.1. Preparation of onion-like carbon (OLC)

OLC are obtained under N<sub>2</sub> atmosphere at 1100 °C, 1400 °C and 1600 °C for 30 min. OLC powder are further modified for carboxylation to increase solubility as previously described. In brief, OLC powder immersed in an acid mixture (H<sub>2</sub>SO<sub>4</sub>:HNO<sub>3</sub> =3:1(v: v)) at 80 °C for 24 h. The treated OLC is washed by ultrapure water for several times to pH = 7 and dried in air. Then OLC powder are grinded with NaCl and dispensed in water for ultrasonic treatment. Finally, the mixture is centrifuged and washed, and a uniform solution of OLC is obtained. The product is labelled as OLC-1100, OLC-1400 and OLC-1600.

### 2.2.2. Preparation of photocatalysts CN, CN-ND, CN-OLC

Urea (10 g) is dissolved in ultrapure water (20 mL). The solution is stirred 30 min and then kept in liquid nitrogen, followed by freeze drying. Then obtained precursors is put into a crucible with a cover and annealed in muffle furnace at 550 °C for 2 h at a ramp rate of 2 °C/min. The product is denoted as CN. The steps for the preparation of CN-OLC are similar to those for CN, except different amounts of onion-like carbon are added into solution. The product is labelled as CN-OLC-X, where X represented the initial mass of OLC-1400. The synthesized methods of CN-ND or CN-CQDs is same as CN-OLC.

## 2.3. Characterization

X-ray diffraction (XRD) pattern is obtained on a Bruker DAVINCI D8 Focus diffractometer equipped with Cu K $\alpha$  radiation to characterize crystal structure. The morphology is investigated by field emission scanning electron microscopy (SEM, Hitachi S4800) and high-resolution transmission electron microscopic (HRTEM, JEM-2100F). UV-vis diffuse reflectance spectra are performed on UV-VIS-NIR spectrophotometer (Cary7000, Agilent, BaSO<sub>4</sub> as reference) to evaluate light absorption capacity. Raman spectroscopy and Fourier transform infrared spectroscopy (FTIR) are respectively constructed at a confocal microscope-based Raman spectrometer (InVia-Reflex, Renishaw) with an excitation light at 532 nm and FTIR spectrometer (Excalibur 3100, Varian). X-ray photoelectron spectroscopy and Ultraviolet photoelectron spectroscopy are conducted at Thermo Scientific ESCALAB 250XI to determine the element valence state and valence band energy, respectively. Photoluminescence (PL) and time-resolved photoluminescence (TRPL) spectra are collected on NanoLOG-TCSPC to detect photoexcited electron transfer. The electron paramagnetic resonance (EPR) spectra are conducted on a Bruker ELEXSYS-II E500 CW-EPR spectrometer for active species monitoring.

## 2.4. Photocatalytic measurements

### 2.4.1. Photocatalytic H<sub>2</sub> evolution Tests

In a typical experiment, photocatalyst (25 mg) are dispersed to ultrapure water (45 mL) with TEOA (5 mL, 10%) as a sacrificial electron donor. Then, 130  $\mu$ L of H<sub>2</sub>PtCl<sub>6</sub> (2 wt% Pt) aqueous solution is added. Before the light irradiation, the suspension is dispersed by ultrasonic treatment for 10 min and evacuated several times to remove the dissolved air. Then, the sealed quartz tube is irradiated in 30 min by using a 300 W Xenon lamp (PLS-SXE300, Beijing Perfectlight Technology Co.

Ltd) for Pt photodeposition. The reaction temperature is stably maintained by using circulating cooling water. During the visible light irradiation, the evolved  $H_2$  is gathered at a specified time interval and analyzed by gas chromatography (Shimadzu, GC-2014C, 5 Å molecular sieve column,  $N_2$  as carrier gas) with a thermal conductivity detector (TCD).

#### 2.4.2. Photocatalytic degradation tests

In a typical test, 20 mg catalyst was placed in 50 mL RhB solution (10 mg/L). Before irradiation, the solution was magnetically stirred in the dark for 30 min to ensure an adsorption/desorption equilibrium. A 300 W xenon lamp (Beijing CEAULIGHT Co., Ltd.) was used as light source with a UV cutoff filter ( $\lambda > 420$  nm). At different time intervals, 1 mL of the sample was collected and test using UV-vis spectrometer. The concentration of RhB was measured according to their maximum absorbance at 554 nm in UV-vis spectra. Before measurement, the suspension was centrifuged in order to remove photocatalyst.

### 3. Results and discussion

#### 3.1. Synthesis approach and structure characterization

OLC was prepared by high-temperature annealing of nanodiamonds (NDs). Fig. 1a shows the typical XRD pattern of the OLC specimen obtained at 1400 °C. One can observe a wide band located at 15–35° and two peaks at 44° and 75°, attributed to (002) planes of graphitized ( $sp^2$ ) carbon and (111) and (220) crystal faces of  $sp^3$  carbon in diamond, respectively. The  $sp^2$ / $sp^3$  hybrid structure was further confirmed by the Raman spectra (Fig. S1), consisting of the disorder-induced double-resonance D-band at 1340  $cm^{-1}$  and the graphite G-band at 1582  $cm^{-1}$ . The morphology of the as-prepared OLC was also characterized by TEM. As shown in Fig. 1c, the OLC are spheroidal particles with a mean size of 5 nm. Moreover, the HRTEM image in Fig. 1b shows that the diamond

cores are covered by multiple concentric graphitic carbon layers. Lattice fringes with distance of 0.34 and 0.206 nm are clearly observed in the out layer and inner core, which are attributed to (002) graphitized carbon and (111) cubic diamond, respectively. OLC are uniform nanoparticles with a size ranging from 3 to 7 nm, whose Gaussian fitting curve reveals an average diameter of 5.25 nm (Fig. 1c, S2).

A high degree of  $sp^2$  carbon ordering is desirable to enhance the electrical conductivity in terms of photocatalysis. In our case, the  $sp^2$  carbon layer of OLC can be fine-tuned by controlling thermal annealing process, such as temperature and duration. XRD and Raman were employed to monitor the structural changes from NDs to OLC induced by thermal annealing at different temperatures. XRD pattern shows the emergence of (002) graphite peak after thermal treatment at temperature of 1100 °C, whose intensity increased as the annealing temperature increased to 1400 °C (Fig. S3). By contrast, the intensity of (111) and (220) diamond peak gradually decreased. The Raman spectrum of pristine NDs show the characteristic peak of diamond located at 1332  $cm^{-1}$ . After annealing at 1100 °C, D- and G-bands of  $sp^2$ -hybridized carbon emerged, overshadowing the diamond band. Raman spectrum of OLC prepared at 1400 °C is dominated by the  $sp^2$ -bonded carbon (D and G bands), revealing the phase transformation of NDs to carbon onion. In addition, TEM images (Fig. S4) clearly show the  $sp^3$ - $sp^2$  phase transformation from outside to inside. The bare NDs precursor show spherical shape with clear lattice fringe of 0.206 nm. Carbon onion shells started to form on the surface of diamond core via thermal annealing, and further increasing the temperature resulted more graphitized carbon shell layers.

Furthermore, g-C<sub>3</sub>N<sub>4</sub> containing different amounts of OLC has been successfully synthesized. The XRD pattern of pure CN shows two distinct characteristic peaks at 13.1° and 27.7°, belonging to (100) crystal plane of tri-s-triazine rings and (002) plane of the interlayer stacking of aromatic structure. After embedding OLC nanoparticles, the diffraction peaks of g-C<sub>3</sub>N<sub>4</sub> remain unchanged, and a weak peak attributed to the

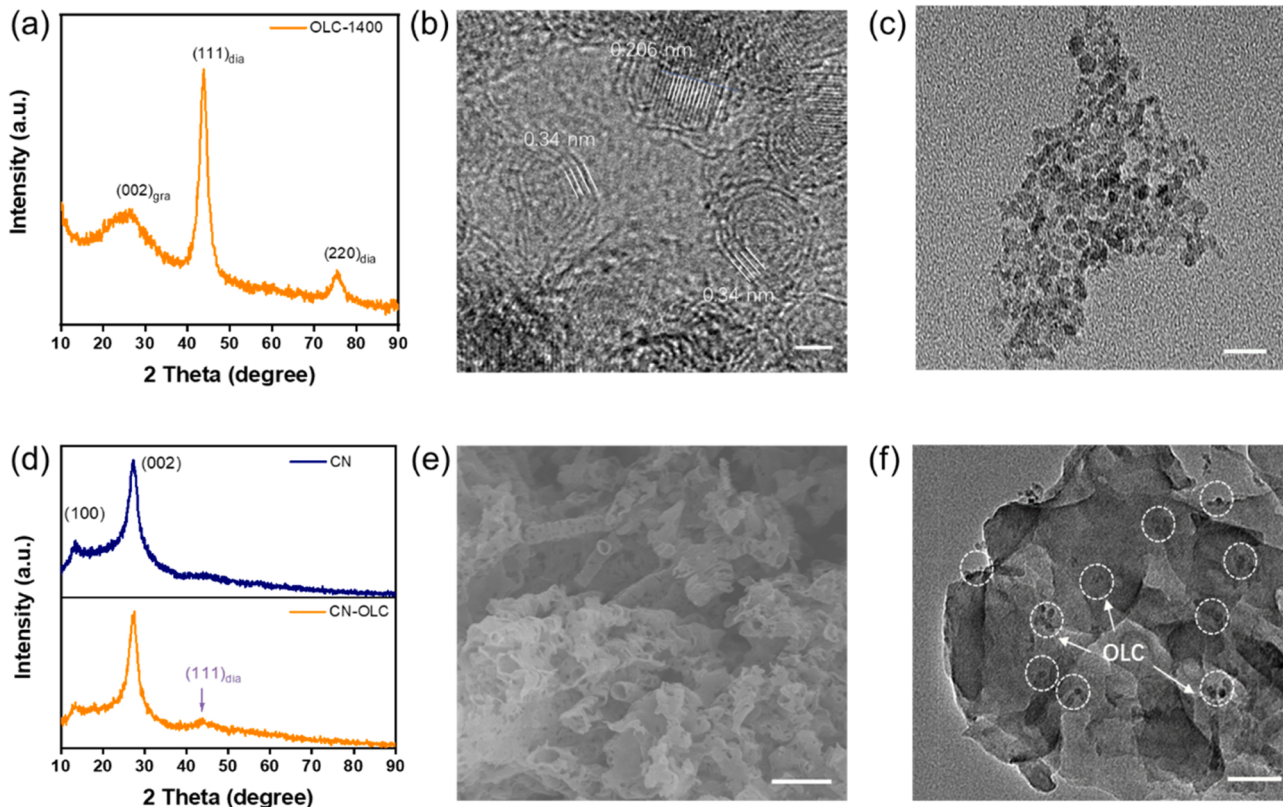


Fig. 1. (a) XRD patterns of OLC-1400. (b, c) HRTEM and TEM images of OLC-1400. (d) XRD patterns of CN and CN-OLC. (e, f) SEM and TEM images of CN-OLC-5. Scale bars: (b) 2 nm, (c) 20 nm, (e) 1  $\mu$ m and (f) 50 nm.

(111) plane of diamonds was observed (Fig. 1d). Element analysis shows that g-C<sub>3</sub>N<sub>4</sub> and CN-OLC are mainly composed of carbon and nitrogen. The C and N content ratio (C/N) ranged from 0.66 to 0.73 with increasing the OLC amount during the preparation of CN-OLC sample (Table S1).

As shown in SEM images (Fig. 1e, S5), the g-C<sub>3</sub>N<sub>4</sub> and CN-OLC exhibit lamellar microstructure with abundant pores, together with hollow nanotubes. The above-mentioned structures are able to enhance light scattering and prolong light dwell time compared to bulk CN, which in turn enhances light absorption. Specific surface area prepared by different methods was revealed by nitrogen adsorption-desorption isotherm. Larger surface areas can be obtained by freeze-drying methods (78.66 m<sup>2</sup>/g) than normal high-temperature drying (47.19 m<sup>2</sup>/g), which provides more reaction sites (Fig. S6). Close observation of the HRTEM image of the CN-OLC (Fig. 1f) show that lots of OLC particles are distributed on the g-C<sub>3</sub>N<sub>4</sub> sheets without significant agglomeration. Those experimental results explicitly demonstrate that the OLC have been incorporated in the g-C<sub>3</sub>N<sub>4</sub> matrix to form CN-OLC composite.

FTIR spectra and solid-state <sup>13</sup>C nuclear magnetic resonance (NMR) spectra are characterized to evaluate the changes of molecular structure. For g-C<sub>3</sub>N<sub>4</sub> and CN-OLC samples with various OLC content, their FTIR absorption spectra show vibration bands at 810 cm<sup>-1</sup>, 1200–1650 cm<sup>-1</sup>, 3000–3500 cm<sup>-1</sup>, ascribed to stretching vibration of tri-s-triazine ring units, stretching vibration of C-N heterocycles, and N-H bond stretching vibration, respectively (Fig. S8). No additional peaks cause by OLC embedding was detected. Moreover, the solid-state <sup>13</sup>C nuclear magnetic resonance (NMR) spectra of g-C<sub>3</sub>N<sub>4</sub> and CN-OLC demonstrate similar patterns (Fig. S9), implying that incorporation of OLC did not affect tri-triazine-based structure of g-C<sub>3</sub>N<sub>4</sub>. On basis of the chemical composition and structure of OLC and g-C<sub>3</sub>N<sub>4</sub>, we conjecture that the OLC bonded with g-C<sub>3</sub>N<sub>4</sub> sheets by  $\pi$ - $\pi$  stacking. As is known, there are a large range of conjugated planar structures in the tri-s-triazine structure of the g-C<sub>3</sub>N<sub>4</sub> [48], while the sp<sup>2</sup> graphitized carbon on the shell of the OLC also has a large  $\pi$ -conjugated structure [49]. This would result in a strong  $\pi$ - $\pi$  interaction between OLC and g-C<sub>3</sub>N<sub>4</sub>, similar to the interaction between graphene and g-C<sub>3</sub>N<sub>4</sub>.

The chemical states of elements in CN-OLC samples and interaction between OLC and g-C<sub>3</sub>N<sub>4</sub> are considered to influence the separation and recombination of photo-generated carriers, which were analyzed by X-ray photoelectron spectroscopy (XPS). The full spectrum in Fig. 2a shows that the major constituent elements in g-C<sub>3</sub>N<sub>4</sub> and CN-OLC are C and N, as well as a small amount of O. The high-resolution spectrum of C1s in g-C<sub>3</sub>N<sub>4</sub> is deconvoluted into two peaks located at 284.8 eV and 288.2 eV (Fig. 2b), apportioning to the graphitic carbon (C-C) and sp<sup>2</sup>-hybridized carbon in heterocycle (N-C=N). Noteworthily, the peak area ratio of C-C in the CN-OLC specimen increased from 3.67% to 5.51%

compared to g-C<sub>3</sub>N<sub>4</sub> sample (Table S3). Besides, a new peak at 285.0 eV is related to the C-O bond originating from OLC surface oxygen-containing group, indicating a successful incorporation of OLC in g-C<sub>3</sub>N<sub>4</sub>. At the same time, more distinct O peak in the CN-OLC-5 sample is also potent evidence to prove it. In the high-resolution spectrum of N 1s (Fig. 2c), three fitted peaks at 398.8, 400.0 and 401.3 eV can be assigned to sp<sup>2</sup>-bonded nitrogen in triazine rings (C-N=C), the tertiary N atoms in N-(C)<sub>3</sub>, and C-N-H bonding, respectively. The weak peak at 404.0 eV is attributed to the charge effects from low to high energy. The percentage of C=N-C, N-(C)<sub>3</sub> and C-NH<sub>x</sub> bonding in N 1s is listed in Table S2. The higher proportion of Pyrrolic N [N-(C)<sub>3</sub>] in CN-OLC sample verifies that an effective higher density electron cloud is introduced into the conjugated system, which is strong evidence for improved photocatalytic activity [21]. Furthermore, degree of polymerization (DP) of g-C<sub>3</sub>N<sub>4</sub>, which can be expressed by the ratio of sp<sup>2</sup>-N/sp<sup>3</sup>-N, is also a factor affecting catalytic activity. DP of CN-OLC-5 (1.99) is lower than that of CN (2.67), meaning more structure defects are established in CN-OLC-5 as reactive sites for enhanced activity.

Semiconductor light absorption properties tend to limit the catalytic effect, and a broad absorption spectrum often means that more electrons are excited. The optical absorption capacity of pure g-C<sub>3</sub>N<sub>4</sub> and CN-OLC were analyzed by UV-Vis diffuse reflectance spectra (DRS), and the energy band gaps were calculated through the Kudelka-Munk function. As shown in Fig. 3a, the absorption edge of pure g-C<sub>3</sub>N<sub>4</sub> is about 460 nm, corresponding to the energy band gap (Eg) of 2.70 eV (Fig. S10, Table S3). After incorporation of OLC, the absorption range redshifts to 470 nm and its energy band gap is reduced to 2.64 eV, probably due to the quantum confinement effect of the OLC. Besides, the CN-OLC sample has an enhanced absorption band in a wide range of 470–800 nm compared to g-C<sub>3</sub>N<sub>4</sub>. The broaden adsorption band and narrowed band gap of CN-OLC improves its ability to harvest visible light and generate photocarrier, further leading to an enhanced photocatalytic activity.

In addition to the band gap, position of the valence band and the conduction band are also essentially important for a photocatalyst. UV photoelectron spectroscopy (UPS) is characterized to evaluated the valence band structures of g-C<sub>3</sub>N<sub>4</sub>. As shown in Fig. 3b, the valance band (E<sub>VB</sub>) edge position of g-C<sub>3</sub>N<sub>4</sub> and CN-OLC nanosheets were determined to be 1.69 eV and 1.72 eV (Table S4). The conduction band (E<sub>CB</sub>) edge positions of g-C<sub>3</sub>N<sub>4</sub> and CN-OLC were calculated to be -1.01 eV and -0.90 eV by subtracting the Eg values. Accordingly, the band diagrams of g-C<sub>3</sub>N<sub>4</sub> and CN-OLC can be established, as illustrated in Fig. 3c. The E<sub>CB</sub> of CN-OLC is more positive potential than g-C<sub>3</sub>N<sub>4</sub>, meaning that CN-OLC is more thermodynamically beneficial for boosting hydrogen proton reduction due to more rational electron energy level.

Density functional theory (DFT) calculation is employed to investigate the effect of OLC incorporation on band structure. Electron density of VB is mainly composed of N-p orbital while C-p and N-p contribute

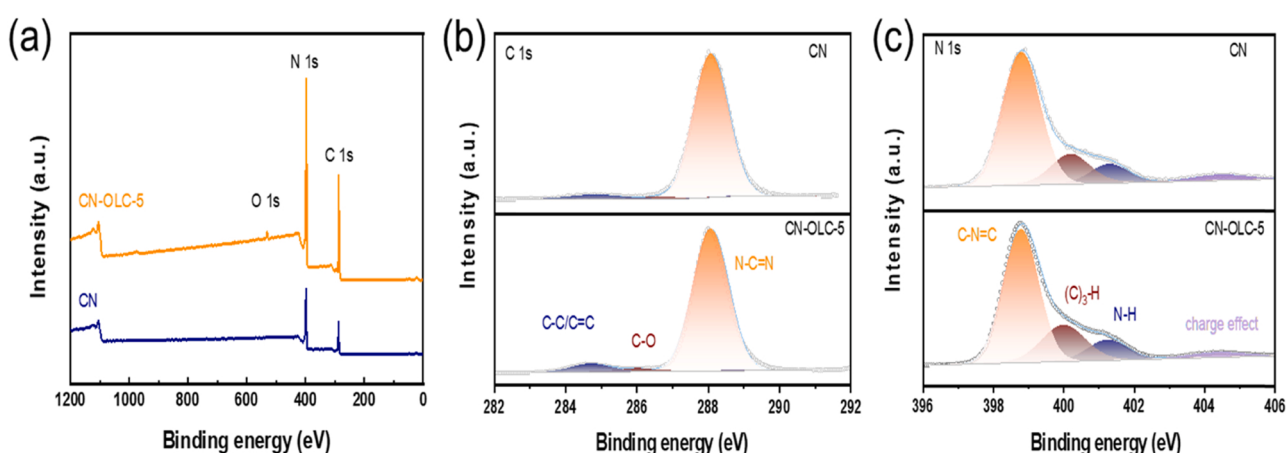
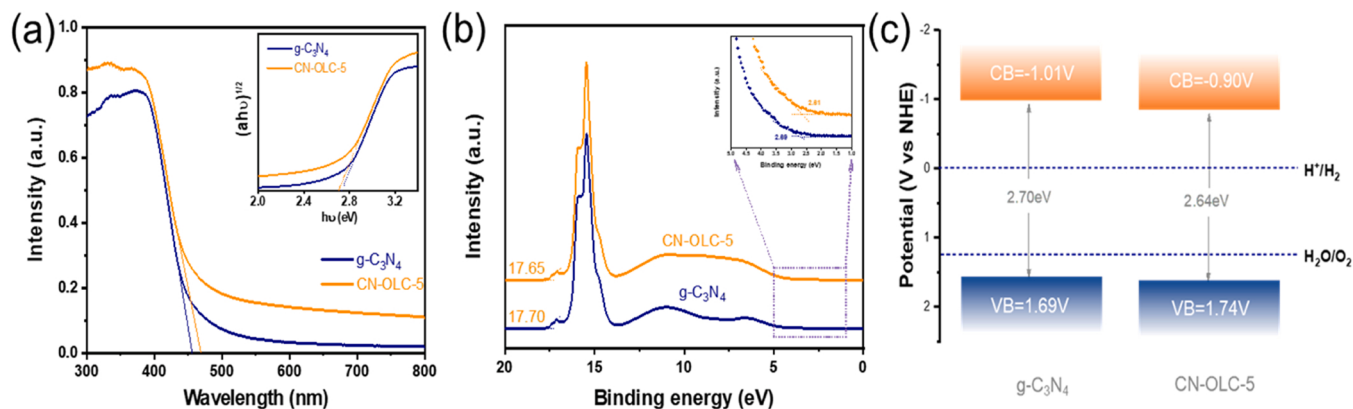


Fig. 2. XPS survey spectra (a) and High-resolution XPS spectra of CN and CN-OLC-5 for C 1s (b) and N 1s (c).



**Fig. 3.** (a) UV–vis absorption spectra of g-C<sub>3</sub>N<sub>4</sub> with OLC (inset: calculated band gap energies). (b, c) UPS spectra and band structure of alignments for g-C<sub>3</sub>N<sub>4</sub> and CN-OLC-5.

collectively to CB as previously reported [50].

The optimized C-doped model of CN-OLC (0.50 eV) shows a narrower gap than pristine g-C<sub>3</sub>N<sub>4</sub> (2.39 eV), which is consistent with DRS results aforementioned (Fig. 3a). The calculated band gaps of the CN-OLC and g-C<sub>3</sub>N<sub>4</sub> are both smaller than that of the experimental values (g-C<sub>3</sub>N<sub>4</sub>: 2.70 eV; CN-OLC: 2.64 eV) due to the limitation of DFT method. Moreover, the distinct decrease of CB minimum is observed, accordance with calculated results from UPS and DRS. Ameliorative electronic property is confirmed with narrow band gap and more positive CB, which will greatly promote photocatalytic reaction efficiency (Fig. 4).

### 3.2. Photocatalytic performance

The photocatalytic HER performance of as-synthesized photocatalysts are evaluated under visible-light ( $\lambda > 420$  nm) with triethanolamine as sacrificial agent and Pt as co-catalyst (Fig. S11). No H<sub>2</sub> was produced for OLC sample, and the H<sub>2</sub> evolution rate of pure g-C<sub>3</sub>N<sub>4</sub> sample is 695  $\mu\text{mol g}^{-1} \text{h}^{-1}$ . After integrating g-C<sub>3</sub>N<sub>4</sub> with 5 mg OLC, HER of CN-OLC increased to 3086  $\mu\text{mol g}^{-1} \text{h}^{-1}$ , which is 4.44 times higher than that of pristine g-C<sub>3</sub>N<sub>4</sub> (Fig. 5a). Further increasing OLC addition amount to 10 mg and 20 mg, the photocatalytic activity of the CN-OLC decreased to 1460 and 1085  $\mu\text{mol g}^{-1} \text{h}^{-1}$ . Herein, a moderate amount of OLC can facilitate visible light adsorption and serve as

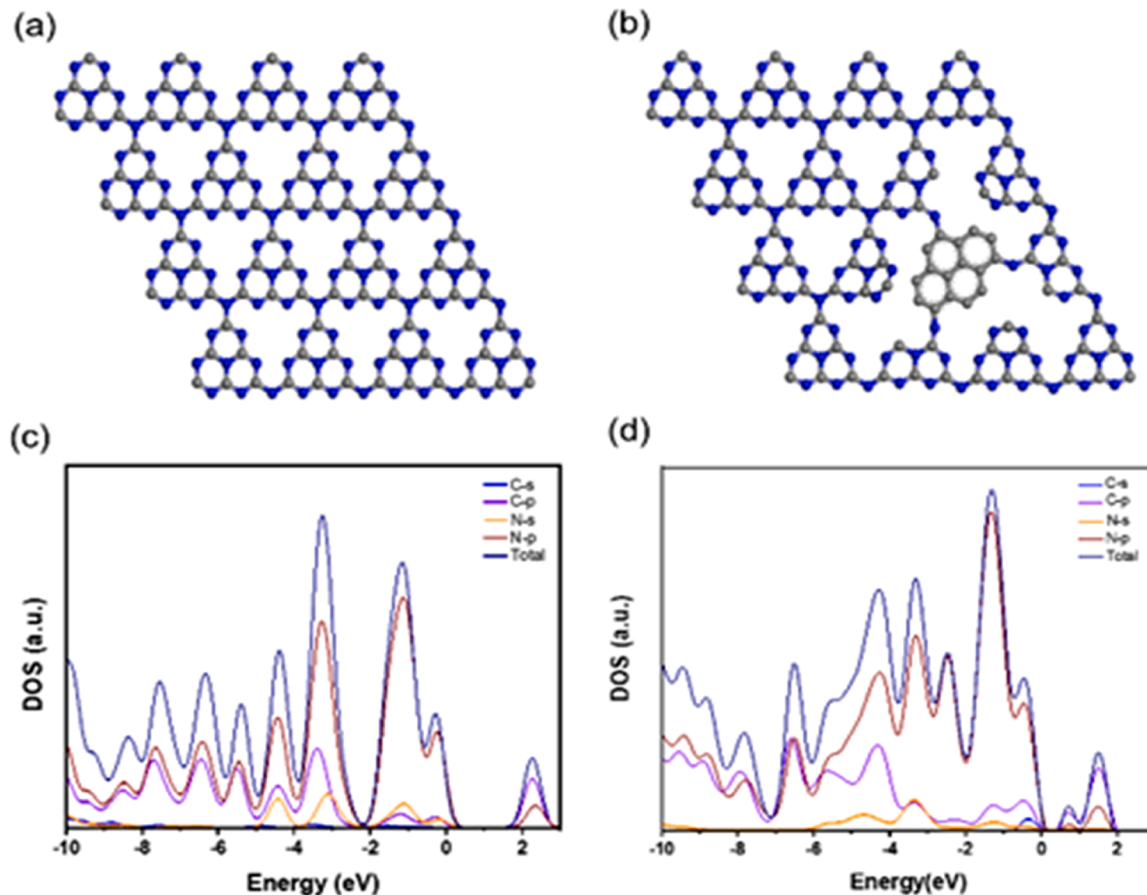


**Fig. 4.** Optimized unit cells and calculated density of states for C<sub>3</sub>N<sub>4</sub> (a, c) and C-C<sub>3</sub>N<sub>4</sub> (b, d).

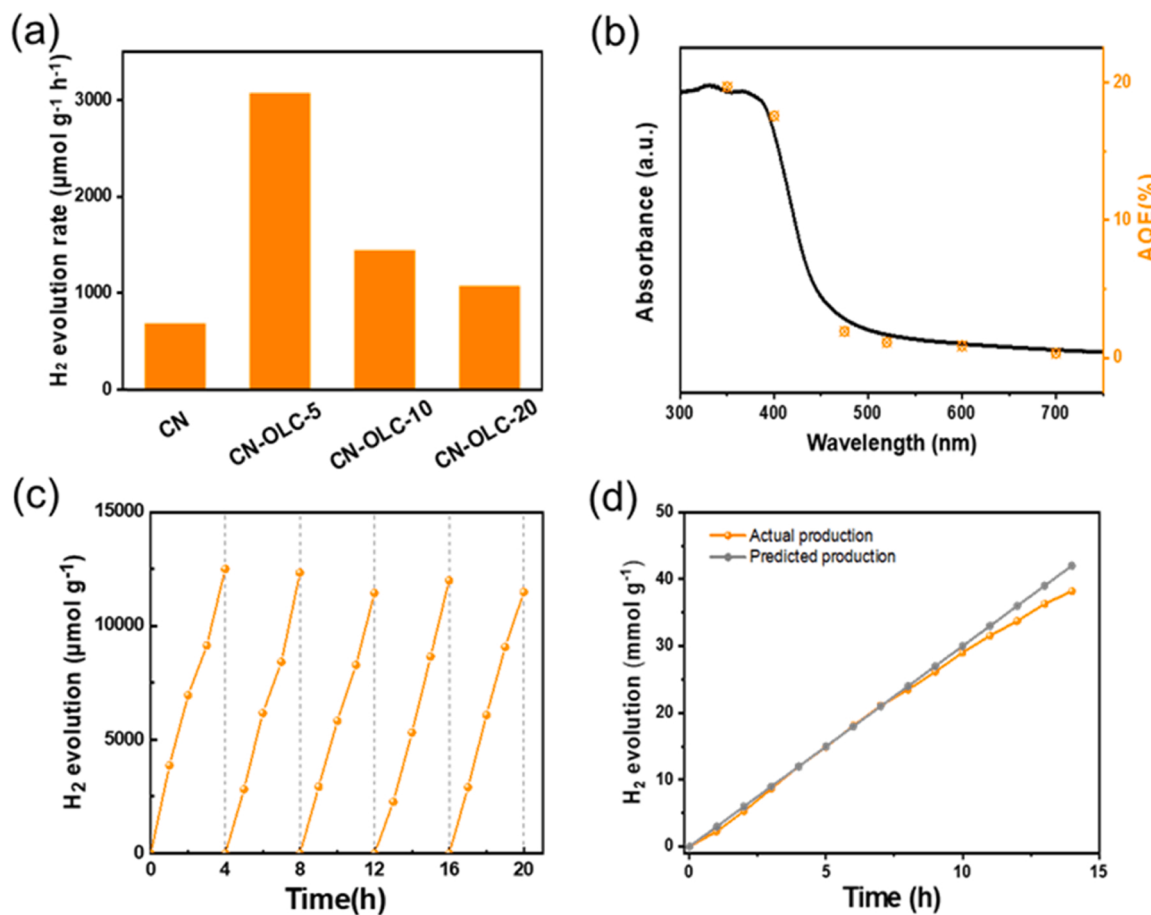


**Fig. 5.** (a) H<sub>2</sub> evolution amounts of CN with different amount of OLC. (b) Absorption-spectra-dependent AQE of CN-OLC-5. (c) Cycling experiments of photocatalysis H<sub>2</sub> evolution of CN-OLC-5. (d) Comparison of actual and predicted yields of CN-OLC-5.

electronic media to accelerate photo-induced electron transfer efficiency. However, excess carbonous component may adversely shield the light absorption and become photo-electrons/holes recombination centers. In addition, excessive loading of OLC could break tri-s-triazine skeleton of g-C<sub>3</sub>N<sub>4</sub>, thereby decreasing the hydrogen evolution activity. Beside from the loading amount of OLC, homogeneous distribution of OLC in the g-C<sub>3</sub>N<sub>4</sub> is another factor for efficient photo-carriers transfer. In our case, thermal polymerization was utilized to construct CN-OLC heterostructure, rather than physical mixture or electrostatic adsorption. As a comparison, the physical mixture of OLC and g-C<sub>3</sub>N<sub>4</sub> (Fig. S12) show relatively lower H<sub>2</sub> generation rate (948 μmol g<sup>-1</sup> h<sup>-1</sup>). This may be attributed to the agglomeration of OLC, leading to limited active interface and inefficient electrons/holes separation.

Photocatalytic stability is also an important parameter to evaluate catalyst performance in practice. As shown in Figure 5c, H<sub>2</sub> production remains stable in five cycles (4 h for each cycle) without significant deactivation. After continuous photocatalytic tests up to 14 h, the actual yield curve is still comparable to the predicted yield curve, further verifying the long-term stability of CN-OLC catalyst (Fig. 5d). The decrease of H<sub>2</sub> production in later stage may be due to that H<sub>2</sub> concentration or pressure in the reactor gradually increases or H<sub>2</sub> concentration in solution tends to be saturated. Meanwhile, XRD and XPS characterization were carried out to verify whether there were any structural changes after cycle test. From the XRD patterns, one can tell that the intensity of diffraction peak belonging to OLC (20=44°) are unchanged (Fig. S13a) after the tests. Based on the XPS results, the proportion of C and N element was maintained stably (Table S5). These results confirm the structural stability of CN-OLC after five cycles (Fig. S13, Table S5). The apparent quantum efficiency (AQE) is

calculated to be 17.57% at  $\lambda = 400$  nm and drops to be about 1.94% at  $\lambda = 475$  nm (Fig. 5b, Table S6). The AQE at different wavelength almost coincides with the light absorption curve. These results demonstrate that as-prepared CN-OLC photocatalyst has a high photocatalytic activity and superior durability.

### 3.3. Photocatalytic mechanism

To shed light on the catalytic mechanism, spectrochemical and photochemical tests are constructed. Generally, photoluminescence (PL) originates from the recombination of charge carriers, and a lower PL intensity indicates suppressed charge recombination. As shown in Fig. 6a, the pristine g-C<sub>3</sub>N<sub>4</sub> exhibits an emission band peaking at 438 nm under excitation of 365 nm, corresponding to band-to-band recombination. For the CN-OLC, the emission peak red-shifts to 460 nm with a weaker PL intensity in comparison with g-C<sub>3</sub>N<sub>4</sub> and physical mixture of OLC and g-C<sub>3</sub>N<sub>4</sub> (Fig. S14). This suggests that the incorporated OLC have narrowed the bandgap and accelerated separation of photo-induced electron-hole pairs, accordance with the experimental results aforementioned. Furthermore, the lifetime of charge carrier, monitored by TRPL, is also strong evidence to evaluate electron-hole separation efficiency after light excitation. The average lifetime was calculated by third-order exponential equation fitting (Fig. 6b, Table S7):

$$I(t) = A_1 \cdot \exp\left(\frac{-t}{\tau_1}\right) + A_2 \cdot \exp\left(\frac{-t}{\tau_2}\right) + A_3 \cdot \exp\left(\frac{-t}{\tau_3}\right) \quad (1)$$

$$\tau_n = \frac{A_1 \tau_1^2 + A_2 \tau_2^2 + A_3 \tau_3^2}{A_1 \tau_1 + A_2 \tau_2 + A_3 \tau_3} \quad (2)$$

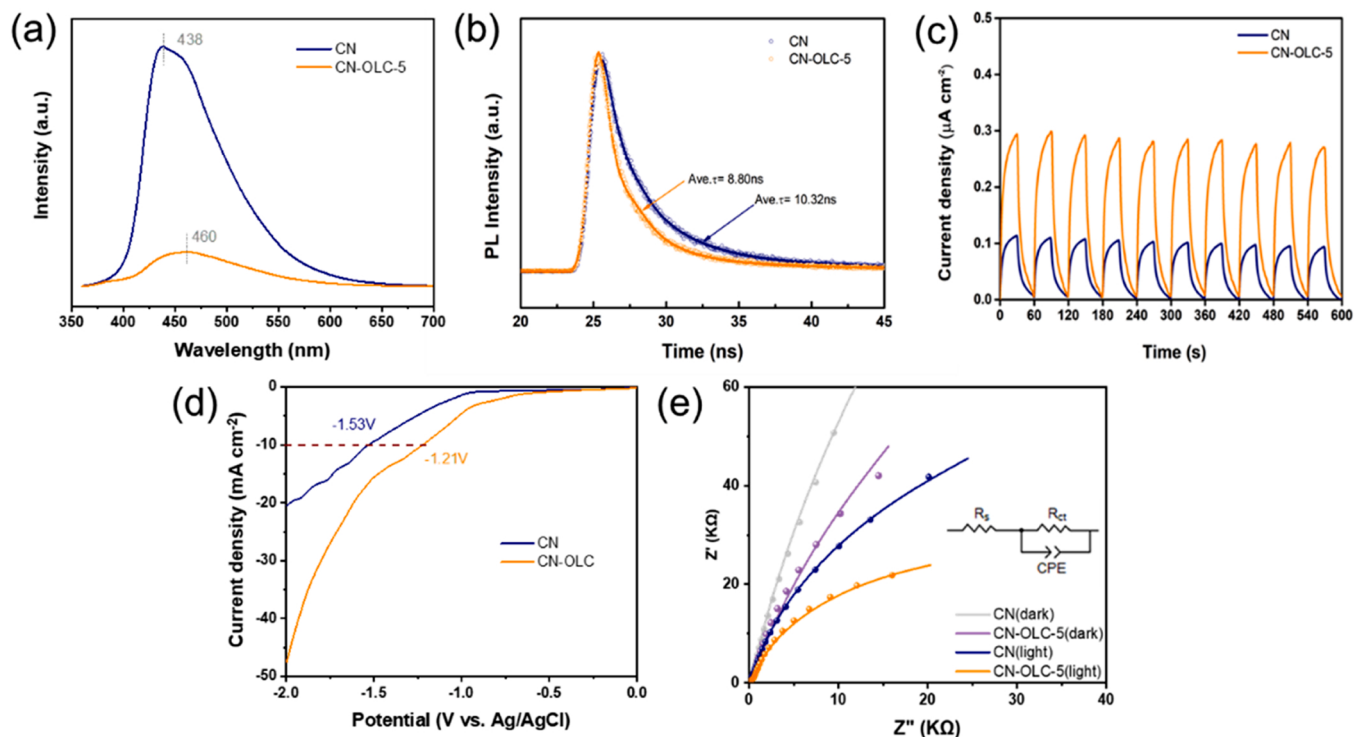


Fig. 6. PL spectra (a), Time-resolved transient PL decay (b), Photocurrent response (c), Linear sweep voltammetry curves (d), EIS Nyquist (e) of CN and CN-OLC-5.

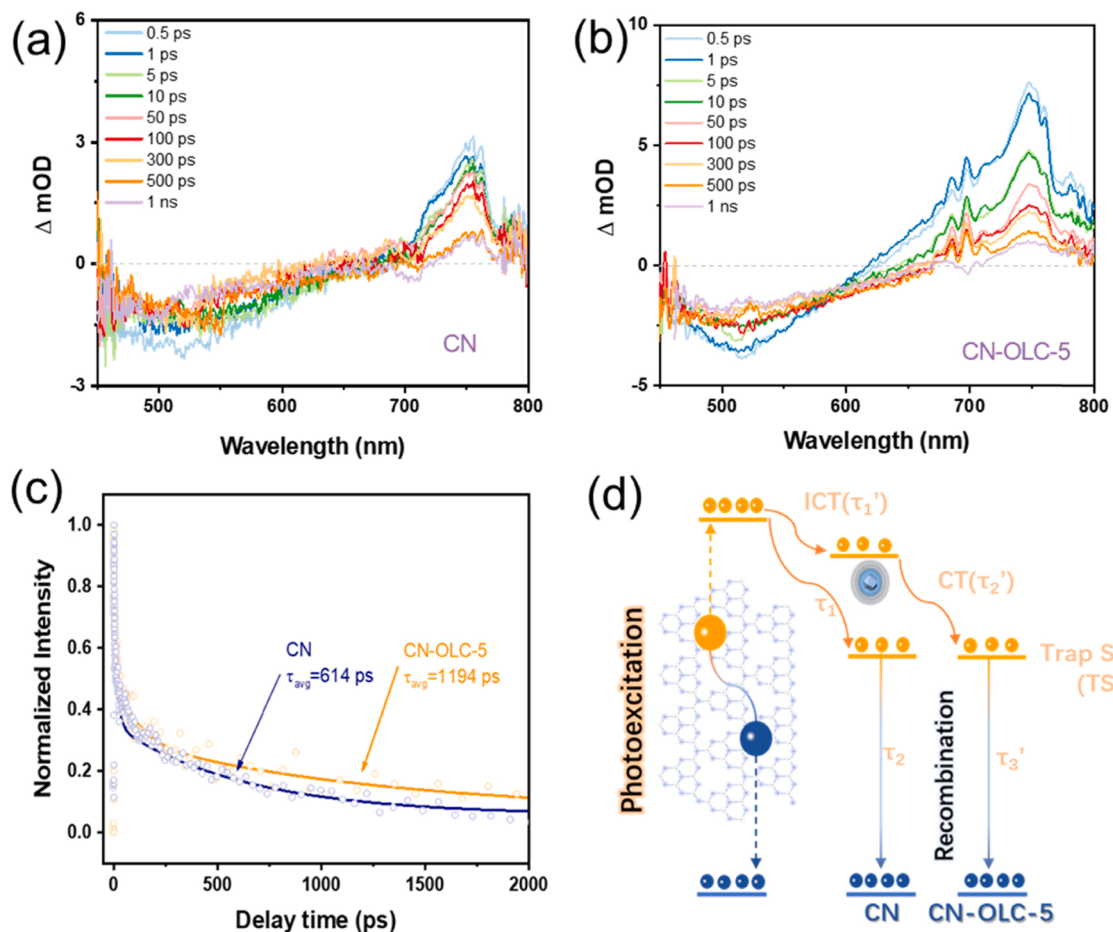


Fig. 7. TA spectra of CN (a) and CN-OLC-5 (b). (c) The normalized fs-TA decay kinetics of CN and CN-OLC-5 probed at 751 nm under 352 nm photo-excitation. (d) Proposed process for charge transfer.

The decay life time of CN-OLC is determined to be 10.32 ns, longer than that of pure g-C<sub>3</sub>N<sub>4</sub> (8.80 ns). The prolonged lifetime reflects that the excited carrier is transferred in time before recombination. Thanks to the excellent electrical conductivity and electron migration rate, the uniformly dispersed OLC as an electron acceptor can transfer electrons in a timely manner, which greatly reduces the recombination of electrons and holes at the excitation site. Decrease of photoluminescence intensity and prolongation of fluorescence lifetime indicates that fewer electrons recombine with holes back to the ground state while more electrons are involved in reduction reaction of non-radiative transition.

In addition, the photocurrent density of CN-OLC (0.30  $\mu\text{A cm}^{-2}$ ) is nearly three times higher than that of pristine g-C<sub>3</sub>N<sub>4</sub> (0.11  $\mu\text{A cm}^{-2}$ ), indicating that more charge carriers were generated and separated in the OLC-embed sample (Fig. 6c). More positive onset potential and smaller overpotential after incorporation signifies higher catalytic activity and more advantageous HER kinetics (Fig. 6d). CN-OLC-5 under illumination exhibits the smallest radius as seen in the impedance plots (Fig. 6e, Table S8). The large amount of graphitized carbon in OLC surface can greatly improve the conductivity, which is main reason for rapid transfer and separation of carriers.

Ultrafast transient absorption spectroscopy is employed to unveil charge transport processes in detail to compare the carrier dynamics between CN and CN-OLC-5. As shown in Fig. 7a and b, both samples exhibit an instantaneous response to the excitation light. The intensity of the absorbed signal weakens significantly with time, indicating the depletion of charge carrier. Furthermore, the continuous negative

absorption ranging from 450 to 620 nm was assigned to the stimulated emission and photobleaching, while an obvious band (620–800 nm) in positive region appears due to the excited-state absorption. The kinetic decay curves are fitted at 751 nm with third-order exponential equation where maximum absorption magnitude is recorded (Fig. 7c, Table S9).

Two apparent processes were identified for pristine g-C<sub>3</sub>N<sub>4</sub>, shorter lifetime ( $\tau_1 = 18$  ps) can be assigned to charge transfer (CT) process from CB to trap state (TS) while another longer lifetime ( $\tau_2 = 631$  ps) is ascribed to charge carrier recombination. For CN-OLC-5, two prolonged components ( $\tau_2' = 98$  ps and  $\tau_3' = 1279$  ps) were obtained than pristine g-C<sub>3</sub>N<sub>4</sub>. Due to doping of OLC, increased defect density of CN was verified by DP, resulting in extended lifetime in CT process ( $\tau_{\text{CT}} =$ from 18 ps to 98 ps). Meanwhile, it is undoubtable to obtain a prolonged lifetime ( $\tau_{\text{recombination}} =$ from 631 ps to 1279 ps) on account of enhanced the carrier separation efficiency, which is corresponding to variations in PL intensity. Moreover, an additional short-lived component ( $\tau_1' = 9.6$  ps) was noticed, which is attributed to intermolecular charge transfer (ICT) between g-C<sub>3</sub>N<sub>4</sub> and OLC. Therefore, CN-OLC-5 exhibits prolonged average lifetime ( $\tau_{\text{avg}} = 1194$  ps) than CN ( $\tau_{\text{avg}} = 614$  ps), indicating more electrons remain at high-excited state for improved photocatalytic activity.

RhB degradation tests are also conducted to evaluate the photocatalytic performance. As shown in Fig. 8a, pseudo-first-order kinetic model is used to calculate the photocatalytic reaction rate constant of the catalyst. The degradation rate of CN-OLC ( $0.1171 \text{ min}^{-1}$ ) demonstrates is 2.5 times higher than that of CN ( $0.04626 \text{ min}^{-1}$ ). Higher rate

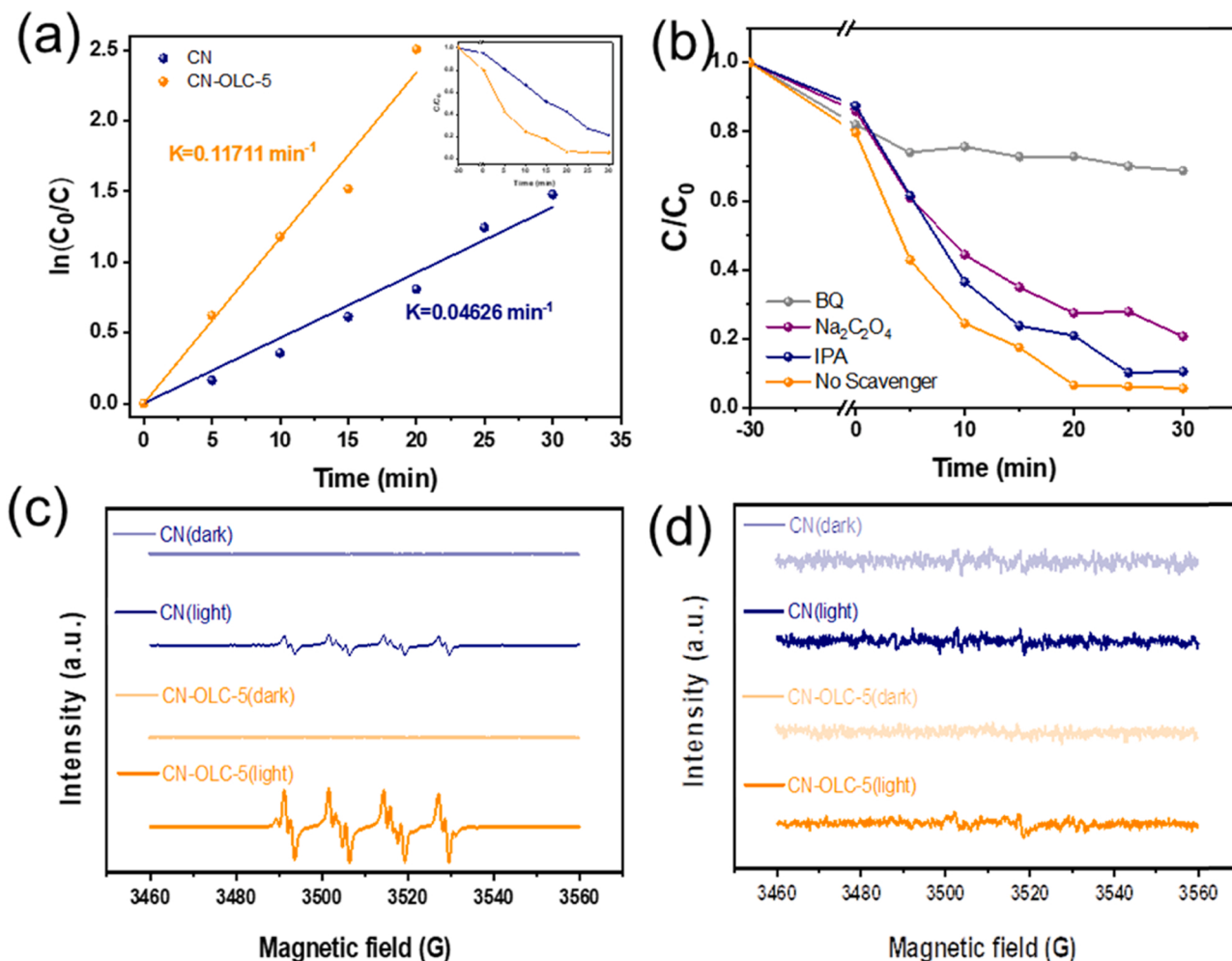


Fig. 8. (a) Calculated rate constant of CN and CN-OLC-5 (inset: photocatalytic degradation efficiencies). (b) RhB photodegradation experiment of CN-OLC-5 with different sacrifices. EPR spectra of CN and CN-OLC-5 (c)  $\bullet\text{O}_2^-$ , (d)  $\bullet\text{OH}$ .

constant generally means more active species, which reveals that OLC plays an essential role in improving photocatalytic activity. To search for which active species are the main contributors to degradation, sacrifices (BQ for singlet oxygen ( $\bullet\text{O}_2^-$ ),  $\text{Na}_2\text{C}_2\text{O}_4$  for holes ( $\text{h}^+$ ), IPA for hydroxyl radicals ( $\bullet\text{OH}$ )) for different active species are introduced. The photodegradation activity was significantly inhibited in the presence of BQ, while the addition of  $\text{Na}_2\text{C}_2\text{O}_4$  and IPA have slightly influence on the photodegradation behavior (Fig. 8b, S15). This signifies that  $\bullet\text{O}_2^-$  is mainly involved in the whole photocatalytic process, rather than  $\text{h}^+$  or  $\bullet\text{OH}$ . To give more understanding about the active species, EPR spectra was established. When the spin probes capture the active species produced by the photocatalyst, the unique peak shape of the active species will appear, while  $\bullet\text{OH}$  corresponds to 1:2:2:1 four characteristic peaks and  $\bullet\text{O}_2^-$  corresponds to 1:1:1:1. Only characteristic signals of  $\bullet\text{O}_2^-$  are detected in the EPR tests, indicating that  $\bullet\text{O}_2^-$  is the main participating species in the degradation process, in accordance with the experiment of sacrificial agent. In addition, CN-OLC-5 shows higher signal intensity than CN under identical irradiation conditions, while no characteristic signal is observed in darkness (Fig. 8c-d). Furthermore, the relationship between the signal intensity of free radical and time is also observed (Fig. S16). Undoubtedly, CN-OLC had better production capacity of active species, and its signal intensity is about 4.6 times that of CN within 160 s, indicating that CN-OLC-5 has better carrier separation ability to reduce oxygen to  $\bullet\text{O}_2^-$ .

In order to demonstrate the excellent performance of OLC-1400 composed of  $\text{sp}^2$  and  $\text{sp}^3$  carbon atom, we use same procedure to prepare  $\text{g-C}_3\text{N}_4$  incorporated with different carbonaceous materials: NDs, OLC-1100, OLC-1600, graphene and CQDs (Fig. 9a, Fig. S17-19). HER of  $\text{g-C}_3\text{N}_4$  modified by ND increased to  $1286 \mu\text{mol g}^{-1} \text{h}^{-1}$ , which is similar to previous work [51–53]. Not surprisingly, OLC-1100 has a greater HER-boosting effect to  $1530 \mu\text{mol g}^{-1} \text{h}^{-1}$ , benefiting from higher electrical conductivity than NDs. As discussed above, OLC has higher  $\text{sp}^2$  carbon content than ND, and higher annealing temperature of  $1400^\circ\text{C}$  produced more  $\text{sp}^2$  carbon. Considering that a high content of  $\text{sp}^2$  carbon is beneficial for the electrical conductivity, the OLC-1400 exhibits better photocatalysis performance than ND and OLC-1100. However, CQDs composed of plentiful  $\text{sp}^2$ -carbon atoms shows similar enhancement effect with OLC-1100, whose HER up to  $1531 \mu\text{mol g}^{-1} \text{h}^{-1}$ . We attribute this result to the fact that the graphite layer on the surface of OLC-1400 has a more perfect ordering of  $\text{sp}^2$  carbon atoms compared to CQDs, thus greatly enhancing the electron-hole separation efficiency. On the other hand, the CN-OLC-1400 also show higher HER than CN-graphene (Fig. S19), even graphene is considered to consist of almost 100%  $\text{sp}^2$  carbon. As mentioned above, the  $\text{sp}^2$  carbon affects the conductivity of carbon materials. Thus, we believe the embedded carbon-based particles will serve as a carrier recombination center when the conductivity

exceeds a certain value, eventually reducing the carrier separation efficiency instead. Similarly, the OLC-1600, with higher content of  $\text{sp}^2$  carbon, embedded  $\text{g-C}_3\text{N}_4$  didn't show good enough hydrogen production performance (Fig. S19).

On the basis of the above results, we propose the mechanism of enhanced the photocatalytic activity of  $\text{g-C}_3\text{N}_4$ . First, the freeze-dried precursor assists  $\text{g-C}_3\text{N}_4$  to form a porous vesicular skeleton with enlarged BET area during in-situ thermal polymerization, which enhances light reflection and provides abundant active sites comparing with bulk materials. Second, due to excellent light-harvesting capacity of graphitized carbon in the shell, CN-OLC exhibits broader visible light utilization region with narrowed band gap. Furthermore, the incorporation of OLC changes electronic structure (more positive CB meaning lower transfer barrier) for improved photocatalysis reaction dynamically. Third,  $\text{sp}^2$ -carbon is also proved to be a suitable electron acceptor on account of its high conductivity, which light-excited electron-hole pairs can be transferred into to avoid recombination, leading to longer carrier lifetime as verified in TA results. The above properties can greatly enhance carrier separation of composite samples, thus greatly improving the photocatalytic performance.

#### 4. Conclusion

In summary, an efficient photocatalyst  $\text{g-C}_3\text{N}_4$ -OLC was synthesized by modifying  $\text{g-C}_3\text{N}_4$  with OLC, a carbon nanostructure with high degree of  $\text{sp}^2$  carbon ordering and small size. SEM/TEM images, Raman spectra, and XRD patterns confirm the formation  $\text{sp}^2$ -hybridized carbon in OLC, and demonstrate that the OLC has been incorporated in the  $\text{g-C}_3\text{N}_4$  matrix. UV-Vis diffuse reflectance spectra show that light adsorption of  $\text{g-C}_3\text{N}_4$  was extended in visible range after OLC embedding, and the density functional theory calculation further confirmed the narrower band gap. The  $\text{g-C}_3\text{N}_4$ -OLC composites show a rate of hydrogen evolution up to  $3086 \mu\text{mol g}^{-1} \text{h}^{-1}$ , which is 4.44 times higher than untreated  $\text{g-C}_3\text{N}_4$ . Efficient photocatalytic degradation of RhB was also achieved with rate constant about  $0.1171 \text{ min}^{-1}$ . In particular, the  $\text{H}_2$  evolution rate is highly dependent on the  $\text{sp}^2/\text{sp}^3$  ratio of OLC. Then, photocatalytic mechanism was discussed in detail. Photoluminescence spectra and decay curves prove that the embedded OLC can accelerate separation of photo-induced electron-hole pairs in  $\text{g-C}_3\text{N}_4$ . Ultrafast transient absorption spectroscopy demonstrates that OLC could work as charge reservoir to enhance the carrier separation efficiency. The previous work provides a competitive approach to prepare carbon-based photocatalyst, achieving enhanced photocatalytic hydrogen evolution and dye degradation.

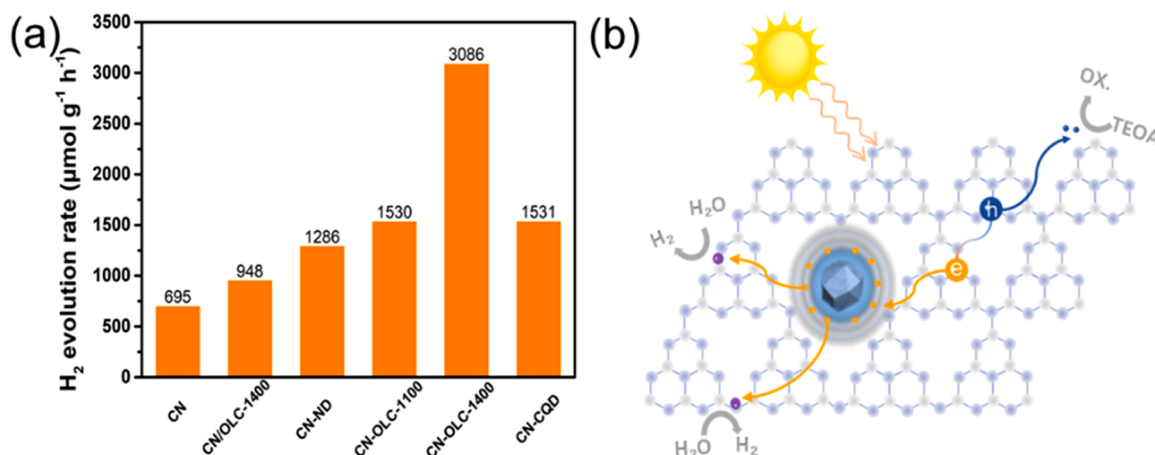


Fig. 9. (a)  $\text{H}_2$  evolution amounts of CN with different carbon materials. (b) Proposed mechanism for enhanced hydrogen evolution.

## CRediT authorship contribution statement

**Yuxi Shi:** Conceptualization, Methodology, Software, Data curation, Writing – original draft, **Qi Zhao:** Visualization, Investigation, Writing – review & editing, **Jiayin Li:** Software, Validation, **Guanyue Gao:** Validation, Investigation, **Jinfang Zhi:** Conceptualization, Writing – review & editing, Supervision, Funding acquisition.

## Declaration of Competing Interest

The authors declare that they have no known competing financial interests or personal relationships that could have appeared to influence the work reported in this paper.

## Acknowledgements

The authors thank the financial support from National Natural Science Foundation of China (No. 21874143) and International Partnership Program of Chinese Academy of Sciences (Grant No. GJHZ1818).

## Appendix A. Supporting information

Supplementary data associated with this article can be found in the online version at [doi:10.1016/j.apcatb.2022.121216](https://doi.org/10.1016/j.apcatb.2022.121216).

## References

- [1] A. Fujishima, K. Honda, Electrochemical photolysis of water at a semiconductor electrode, *Nature* 238 (5358) (1972) 37–38.
- [2] S. Cao, et al., Polymeric photocatalysts based on graphitic carbon nitride, *Adv. Mater.* 27 (13) (2015) 2150–2176.
- [3] W.-J. Ong, et al., Graphitic carbon nitride ( $\text{g-C}_3\text{N}_4$ )-based photocatalysts for artificial photosynthesis and environmental remediation: are we a step closer to achieving sustainability? *Chem. Rev.* 116 (12) (2016) 7159–7329.
- [4] L. Lin, Z. Yu, X. Wang, Crystalline carbon nitride semiconductors for photocatalytic water splitting, *Angew. Chem. Int. Ed.* 58 (19) (2019) 6164–6175.
- [5] F.K. Kessler, et al., Functional carbon nitride materials — design strategies for electrochemical devices. *Nature Reviews Materials* 2 (6) (2017) 17030.
- [6] D. Huang, et al., Megamerger in photocatalytic field: 2D  $\text{g-C}_3\text{N}_4$  nanosheets serve as support of 0D nanomaterials for improving photocatalytic performance. *Appl. Catal. B: Environ.* 240 (2019) 153–173.
- [7] D. Masih, Y. Ma, S. Rohani, Graphitic  $\text{C}_3\text{N}_4$  based noble-metal-free photocatalyst systems: a review, *Appl. Catal. B Environ.* 206 (2017) 556–588.
- [8] F. He, et al., The nonmetal modulation of composition and morphology of  $\text{g-C}_3\text{N}_4$ -based photocatalysts, *Appl. Catal. B Environ.* 269 (2020), 118828.
- [9] F. Zhang, et al., Olefin-linked covalent organic framework nanotubes based on triazine for selective oxidation of sulfides with  $\text{O}_2$  powered by blue light, *Appl. Catal. B Environ.* 305 (2022), 121027.
- [10] H. Hao, et al., 2D  $\text{sp}^2$  carbon-conjugated triazine covalent organic framework photocatalysis for blue light-induced selective oxidation of sulfides with  $\text{O}_2$ , *Appl. Catal. B Environ.* 299 (2021), 120691.
- [11] A. Kudo, Y. Miseki, Heterogeneous photocatalyst materials for water splitting, *Chem. Soc. Rev.* 38 (1) (2009) 253–278.
- [12] M.-Y. Ye, et al., 0D/2D heterojunctions of vanadate quantum dots/graphitic carbon nitride nanosheets for enhanced visible-light-driven photocatalysis, *Angew. Chem. Int. Ed.* 56 (29) (2017) 8407–8411.
- [13] W. Zou, et al., Enhanced visible light photocatalytic hydrogen evolution via cubic  $\text{CeO}_2$  hybridized  $\text{g-C}_3\text{N}_4$  composite, *Appl. Catal. B Environ.* 218 (2017) 51–59.
- [14] L. Shi, et al., Rationally designed  $\text{MoS}_2$ /protonated  $\text{g-C}_3\text{N}_4$  nanosheet composites as photocatalysts with an excellent synergistic effect toward photocatalytic degradation of organic pollutants. *J. Hazard. Mater.* 347 (2018) 431–441.
- [15] H. Yang, et al., Constructing electrostatic self-assembled 2D/2D ultra-thin  $\text{ZnIn}_2\text{S}_4$ /protonated  $\text{g-C}_3\text{N}_4$  heterojunctions for excellent photocatalytic performance under visible light. *Appl. Catal. B Environ.* 256 (2019), 117862.
- [16] X.-H. Jiang, et al., Silver single atom in carbon nitride catalyst for highly efficient photocatalytic hydrogen evolution, *Angew. Chem. Int. Ed.* 59 (51) (2020) 23112–23116.
- [17] L. Zhang, et al., Direct observation of dynamic bond evolution in single-atom Pt/ $\text{C}_3\text{N}_4$  catalysts, *Angew. Chem. Int. Ed.* 59 (15) (2020) 6224–6229.
- [18] G. Liu, et al., Confining single-atom Pd on  $\text{g-C}_3\text{N}_4$  with carbon vacancies towards enhanced photocatalytic NO conversion, *Appl. Catal. B Environ.* 284 (2021), 119683.
- [19] S. Kundu, K. Bramhaiah, S. Bhattacharyya, Carbon-based nanomaterials: in the quest of alternative metal-free photocatalysts for solar water splitting, *Nanoscale Adv.* 2 (11) (2020) 5130–5151.
- [20] X.-L. Pu, et al., Self-assembly of a  $\text{g-C}_3\text{N}_4$ -based 3D aerogel induced by N-modified carbon dots for enhanced photocatalytic hydrogen production. *J. Mater. Chem. A* 9 (39) (2021) 22373–22379.
- [21] M. Han, et al., Carbon Dots-implanted graphitic carbon nitride nanosheets for photocatalysis: simultaneously manipulating carrier transport in inter- and intralayers, *Sol. RRL* 4 (4) (2020), 1900517.
- [22] Y. Huang, et al., Controlling carbon self-doping site of  $\text{g-C}_3\text{N}_4$  for highly enhanced visible-light-driven hydrogen evolution. *Appl. Catal. B: Environ.* 254 (2019) 128–134.
- [23] Y. Yu, et al., Surface engineering for extremely enhanced charge separation and photocatalytic hydrogen evolution on  $\text{g-C}_3\text{N}_4$ , *Adv. Mater.* 30 (9) (2018), 1705060.
- [24] Y. Li, et al., Preparation of carbon-rich  $\text{g-C}_3\text{N}_4$  nanosheets with enhanced visible light utilization for efficient photocatalytic hydrogen production, *Small* 13 (33) (2017), 1701552.
- [25] J. Liu, et al., Metal-free efficient photocatalyst for stable visible water splitting via a two-electron pathway, *Science* 347 (6225) (2015) 970–974.
- [26] G. Zhang, et al., Facile “spot-heating” synthesis of carbon dots/graphitic carbon nitride for solar hydrogen evolution synchronously with contaminant decomposition, *Adv. Funct. Mater.* 28 (14) (2018), 1706462.
- [27] T. Song, et al., Designed synthesis of a porous ultrathin 2D  $\text{CN}@\text{graphene}@\text{CN}$  sandwich structure for superior photocatalytic hydrogen evolution under visible light, *Chem. Eng. J.* 404 (2021), 126455.
- [28] Y. Song, et al., Multifunctional self-assembly 3D  $\text{Ag}/\text{g-C}_3\text{N}_4/\text{RGO}$  aerogel as highly efficient adsorbent and photocatalyst for R6G removal from wastewater, *Appl. Surf. Sci.* 542 (2021), 148584.
- [29] Q. Xu, et al., Making co-condensed amorphous carbon/ $\text{g-C}_3\text{N}_4$  composites with improved visible-light photocatalytic  $\text{H}_2$ -production performance using Pt as cocatalyst. *Carbon* 118 (2017) 241–249.
- [30] K. Li, F.-Y. Su, W.-D. Zhang, Modification of  $\text{g-C}_3\text{N}_4$  nanosheets by carbon quantum dots for highly efficient photocatalytic generation of hydrogen, *Appl. Surf. Sci.* 375 (2016) 110–117.
- [31] N. Dwivedi, et al., Correlation of  $\text{sp}^3$  and  $\text{sp}^2$  fraction of carbon with electrical, optical and nano-mechanical properties of argon-diluted diamond-like carbon films, *Appl. Surf. Sci.* 257 (15) (2011) 6804–6810.
- [32] V. Kuznetsov, et al., Controllable electromagnetic response of onion-like carbon based materials, *Phys. Status Solidi (b)* 245 (10) (2008) 2051–2054.
- [33] S. Osswald, et al., Control of  $\text{sp}^2/\text{sp}^3$  carbon ratio and surface chemistry of nanodiamond powders by selective oxidation in Air, *J. Am. Chem. Soc.* 128 (35) (2006) 11635–11642.
- [34] Y. Lin, et al., Catalysis by hybrid  $\text{sp}^2/\text{sp}^3$  nanodiamonds and their role in the design of advanced nanocarbon materials. *Chem. Soc. Rev.* 47 (22) (2018) 8438–8473.
- [35] D.B. Schüpfer, et al., Monitoring the thermally induced transition from  $\text{sp}^3$ -hybridized to  $\text{sp}^2$ -hybridized carbons, *Carbon* 172 (2021) 214–227.
- [36] C. Portet, G. Yushin, Y. Gogotsi, Electrochemical performance of carbon onions, nanodiamonds, carbon black and multiwalled nanotubes in electrical double layer capacitors, *Carbon* 45 (13) (2007) 2511–2518.
- [37] G.S. Szymański, et al., Correlation between the catalytic and electrocatalytic properties of nitrogen-doped carbon nanoonions and the polarity of the carbon surface: Experimental and theoretical investigations, *Carbon* 151 (2019) 120–129.
- [38] X. Duan, et al., Nanodiamonds in  $\text{sp}^2/\text{sp}^3$  configuration for radical to nonradical oxidation: core-shell layer dependence. *Appl. Catal. B Environ.* 222 (2018) 176–181.
- [39] J. Zang, et al., Graphene growth on nanodiamond as a support for a Pt electrocatalyst in methanol electro-oxidation, *Carbon* 50 (8) (2012) 3032–3038.
- [40] R. Wang, et al., Hybrid nanocarbon as a catalyst for direct dehydrogenation of propane: formation of an active and selective core-shell  $\text{sp}^2/\text{sp}^3$  nanocomposite structure, *Chem. A Eur. J.* 20 (21) (2014) 6324–6331.
- [41] M. Zeiger, et al., Review: carbon onions for electrochemical energy storage, *J. Mater. Chem. A* 4 (9) (2016) 3172–3196.
- [42] J.K. McDonough, et al., Influence of the structure of carbon onions on their electrochemical performance in supercapacitor electrodes, *Carbon* 50 (9) (2012) 3298–3309.
- [43] C. Shu, Y. Lin, D. Su, N-doped onion-like carbon as an efficient oxygen electrode for long-life  $\text{Li}-\text{O}_2$  battery, *J. Mater. Chem. A* 4 (6) (2016) 2128–2136.
- [44] K. Lin, et al., Nanoburil graphites, *Adv. Mater.* 33 (17) (2021), 2007513.
- [45] D. Liu, et al., Atomically dispersed platinum supported on curved carbon supports for efficient electrocatalytic hydrogen evolution, *Nat. Energy* 4 (6) (2019) 512–518.
- [46] D. Pech, et al., Ultrahigh-power micrometre-sized supercapacitors based on onion-like carbon, *Nat. Nanotechnol.* 5 (9) (2010) 651–654.
- [47] X. Duan, et al.,  $\text{sp}^2/\text{sp}^3$  framework from diamond nanocrystals: a key bridge of carbonaceous structure to carbocatalysis. *ACS Catal.* 9 (8) (2019) 7494–7519.
- [48] X. Ma, et al., Probing  $\pi$ - $\pi$  stacking modulation of  $\text{g-C}_3\text{N}_4/\text{graphene}$  heterojunctions and corresponding role of graphene on photocatalytic activity. *J. Colloid Interface Sci.* 508 (2017) 274–281.
- [49] L. Tang, et al., Fabrication of compressible and recyclable macroscopic  $\text{g-C}_3\text{N}_4/\text{GO}$  aerogel hybrids for visible-light harvesting: a promising strategy for water remediation, *Appl. Catal. B: Environ.* 219 (2017) 241–248.
- [50] H. Yu, et al., Alkali-assisted synthesis of nitrogen deficient graphitic carbon nitride with tunable band structures for efficient visible-light-driven hydrogen evolution, *Adv. Mater.* 29 (16) (2017), 1605148.
- [51] L.-X. Su, et al., Effective light scattering and charge separation in nanodiamond- $\text{g-C}_3\text{N}_4$  for enhanced visible-light hydrogen evolution. *Carbon* 139 (2018) 164–171.
- [52] L.-X. Su, et al., Heterostructured boron doped nanodiamonds- $\text{g-C}_3\text{N}_4$  nanocomposites with enhanced photocatalytic capability under visible light irradiation. *Int. J. Hydrog. Energy* 44 (36) (2019) 19805–19815.
- [53] L.-X. Su, et al., Emerging applications of nanodiamonds in photocatalysis, *Funct. Diam.* 1 (1) (2021) 93–109.